

Two-dimensional Dirac fermions and quantum magnetoresistance in CaMnBi_2

Kefeng Wang (王克锋),¹ D. Graf,² Limin Wang (王莉敏),¹ Hechang Lei (雷和畅),¹ S. W. Tozer,² and C. Petrovic¹

¹Condensed Matter Physics and Materials Science Department, Brookhaven National Laboratory, Upton, New York 11973, USA

²National High Magnetic Field Laboratory, Florida State University, Tallahassee, Florida 32306-4005, USA

(Received 30 December 2011; published 18 January 2012)

We report two-dimensional Dirac fermions and quantum magnetoresistance in single crystals of CaMnBi_2 . The nonzero Berry's phase, small cyclotron resonant mass, and first-principles band structure suggest the existence of the Dirac fermions in Bi square nets. The in-plane transverse magnetoresistance exhibits a crossover at a critical field B^* from semiclassical weak-field B^2 dependence to the high-field unsaturated linear magnetoresistance ($\sim 120\%$ in 9 T at 2 K) due to the quantum limit of the Dirac fermions. The temperature dependence of B^* satisfies quadratic behavior, which is attributed to the splitting of linear energy dispersion in high field. Our results demonstrate the existence of two-dimensional Dirac fermions in CaMnBi_2 with Bi square nets.

DOI: [10.1103/PhysRevB.85.041101](https://doi.org/10.1103/PhysRevB.85.041101)

PACS number(s): 72.20.My, 72.80.Jc, 75.47.Np

The magnetoresistance (MR) of condensed matter gives information about the characteristics of the Fermi surface and provides promising candidates for magnetic memory or other spintronic devices.¹⁻³ The normal MR in conventional metals is small because semiclassical transport gives quadratic field-dependent MR in the low-field range which would saturate in the high field.³ Application of a strong magnetic field (B) leads to quantization of the orbital motion and results in quantized Landau levels E_n (LLs). In the extreme quantum limit where only the lowest LL dominates, a large linear MR could be expected.⁴⁻⁸ However, the required magnetic field for the quantum limit in metals with parabolic bands is usually very large because LLs are equidistant. The exceptions are large linear MR in $\text{Ag}_{2-\delta}\text{Te/Se}$ and Bi films below 6 T.⁵⁻⁷ Abrikosov proposed that the linear MR is intimately connected with linear energy dispersion⁴ and recent first-principles calculations confirmed the existence of surface states with a linear energy-momentum relationship, the so-called Dirac fermions.⁹

The distance between the lowest and first LLs of Dirac fermions in a magnetic field is very large. The quantum limit where all of the carriers occupy only the lowest LL is easily realized in relatively small fields.^{10,11} Consequently large linear MR could be achieved. Besides $\text{Ag}_{2-\delta}\text{Te/Se}$, the unsaturated linear MR and other quantum transport phenomena were experimentally observed in other Dirac materials, such as topological insulators (TIs), graphene, and some organic conductors.¹²⁻¹⁶ Recently, highly anisotropic Dirac states were observed in SrMnBi_2 ,¹⁷ where linear energy dispersion originates from the crossing of two Bi $6p_{x,y}$ bands in a double-sized Bi square net, which is a part of $(\text{SrBi})^+$ layer.^{17,18}

In this Rapid Communication, we report the quantum oscillation and magnetoresistant behavior in CaMnBi_2 single crystals with a different layered structure but similar two-dimensional (2D) Bi square nets when compared to SrMnBi_2 . The nonzero Berry's phase, small cyclotron resonant mass, and first-principles band structure suggest the existence of Dirac fermions in the Bi square nets. The quasi-2D in-plane transverse magnetoresistance exhibits a crossover at a critical field B^* from a semiclassical weak-field B^2 dependence to a high-field linear-field dependence. The temperature

dependence of B^* satisfies quadratic behavior attributed to the splitting of linear energy dispersion in a high field.

Single crystals of CaMnBi_2 were grown using a high-temperature self-flux method.¹⁹ Stoichiometric mixtures of Ca (99.99%), Mn (99.9%), and excess Bi (99.99%) with a ratio of Ca : Mn : Bi = 1 : 1 : 9 were sealed in a quartz tube, heated to 1050 °C, and cooled to 450 °C, where the crystals were decanted. The resultant crystals are platelike and the basal plane of a cleaved crystal is the crystallographic ab plane. Electrical transport measurements up to 9 T were conducted in a Quantum Design physical property measurement system (PPMS-9) with a conventional four-wire method. In the in-plane measurements, the current path was in the ab plane, whereas the magnetic field was parallel to the c axis, except in the rotator experiments. In the out-of-plane (c -axis) resistivity measurements, electric current and magnetic fields were parallel to the c axis. High-field MR oscillations up to 35 T were performed at the National High Magnetic Field Laboratory in the same configuration as the in-plane MR. The magnetization measurements were performed in a Quantum Design magnetic property measurement system (MPMS) in both zero-field cooling (ZFC) and field cooling (FC). First-principles electronic structure calculations were performed using experimental lattice parameters within the full-potential linearized augmented plane-wave (LAPW) method²⁰ implemented in the WIEN2K package.²¹ The general gradient approximation (GGA) of Perdew *et al.*²² was used for the exchange-correlation potential.

A CaMnBi_2 unit cell with a $P4/nmmm$ space group contains alternatively stacked two MnBi_4 tetrahedron layers and a 2D Bi square net separated by Ca atoms along the c axis [Fig. 1(a)]. The MnBi_4 tetrahedrons are less distorted and the lattice is smaller when compared to SrMnBi_2 with a $I4/mmm$ space group since Ca has a smaller radius than Sr.^{17,23} The in-plane resistivity $\rho_{ab}(T)$ [Fig. 1(b)] is metallic with a weak anomaly at ~ 50 K. The resistivity along the c axis is higher in magnitude than the in-plane resistivity with $\rho_c(T)/\rho_{ab}(T) \sim 10-15$ below 100 K. In what follows we will only discuss the in-plane MR. An external magnetic field enhances the low-temperature resistivity, and the MR ratio $\text{MR} = [\rho_{ab}(B) - \rho_{ab}(0)]/\rho_{ab}(0)$ reaches 120% at 2 K in a 9-T field. As the temperature is increased, the magnetoresistance

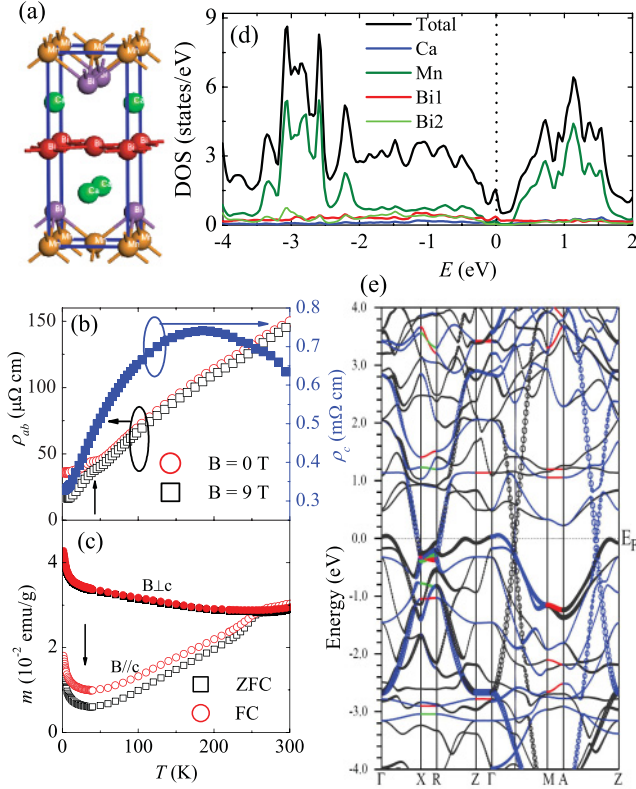


FIG. 1. (Color online) (a) Crystal structures of CaMnBi_2 . Bi atoms in 2D square nets are shown by red balls. Ca atoms are denoted by green balls. Another location of Bi atoms is denoted by purple balls. Mn atoms are denoted by orange balls. Blue lines define the unit cell. (b) Temperature dependence of the in-plane resistivity $\rho_{ab}(T)$ (open symbols) and c -axis resistivity $\rho_c(T)$ (solid symbols) of the CaMnBi_2 single crystal in the $B = 0$ T (squares) and $B = 9$ T (circles) magnetic fields, respectively. (c) Magnetization (M) in $B = 1$ T field applied parallel (open symbols) and perpendicular (solid symbols) to the c axis in both ZFC (squares) and FC (circles) runs. (d) The total DOS and local DOS from Ca, Mn, Bi square nets (Bi1) and Bi in MnBi_4 tetrahedron (Bi2) for AFM CaMnBi_2 . The dotted line indicates the position of the Fermi energy. (e) The band structure for CaMnBi_2 . The heavy lines with circles denote the bands from Bi square nets and the dotted line indicates the position of the Fermi energy.

is gradually suppressed and becomes negligible above ~ 50 K. Magnetization shows a kink at ~ 250 K, indicating an antiferromagnetic (AFM) transition [Fig. 1(d)]. The anomaly in the resistivity at 50 K is clearly not related to the AFM order and is possibly due to the weak ferromagnetic order or impurity scattering since the magnetization shows an upturn around that temperature, which is denoted by the arrow in Fig. 1(c).

The spin-polarized first-principles calculation reveals that the net magnetization in the unit cell is nearly zero, confirming the AFM ground state [Figs. 1(d) and 1(e)]. The structure with a Néel-type AFM configuration in the ab plane has the lowest energy in the first-principles calculation because the MnBi_4 layers are separated by Ca and Bi layers along the c axis and consequently the interlayer coupling is rather weak.^{24,25} The density of states (DOS) at the Fermi level of CaMnBi_2 [Fig. 1(d)] is dominated by the contribution from states in Bi

square nets since the AFM order of Mn ions expels the states of Mn away from the Fermi level. The band structure [Fig. 1(e)] confirms this. There are two narrow bands at the Fermi level with nearly linear energy dispersion along the Γ - M and the A - Z directions, in addition to a wide band along the X - R direction. Hence the 2D Bi square nets of CaMnBi_2 host Dirac states with quasi-2D Fermi surfaces (FSs).

The magnetotransport of solids only responds to the extremal cross section S_F of the Fermi surface along the field direction. For a (quasi)-2D FS, the cross section has $S_F(\theta) = S_0/|\cos(\theta)|$ angular dependence, and 2D states will only respond to perpendicular component of the magnetic field $B|\cos(\theta)|$.³ For example, the 2D states in graphene and the surface states of TIs exhibit $|\cos\theta|$ angular-dependent magnetotransport.^{11,12} The magnetoresistance of CaMnBi_2 shows significant dependence on the field direction (Fig. 2). The crystal was mounted on a rotating stage such that the tilt angle θ between the crystal surface (ab plane) and the magnetic field can be continuously changed with currents flowing in the ab plane perpendicular to magnetic field, as shown in the inset of Fig. 2(a). Angular-dependent magnetoresistance $\rho(B, \theta)$ at $T \sim 2$ K is shown in Figs. 2(b) and 2(c). When B is parallel to the c axis ($\theta = 0^\circ, 180^\circ$), the MR is maximized and is linear in field for high fields. With an increase in the tilt angle θ ,

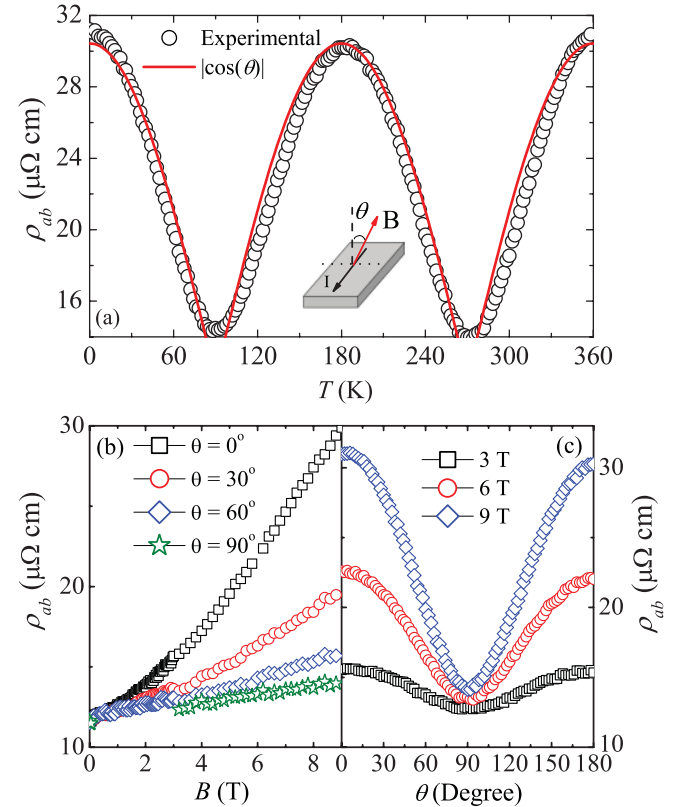


FIG. 2. (Color online) (a) In-plane resistivity ρ vs the tilt angle θ from 0° to 360° at $B = 9$ T and $T = 2$ K for CaMnBi_2 . The red solid line is the fitting curve using $|\cos(\theta)|$ (see text). The inset shows the configuration of the measurement. (b) In-plane resistivity ρ vs magnetic field B of the CaMnBi_2 crystal with different tilt angles θ between the magnetic field and the sample surface (ab plane) at 2 K. (c) ρ vs the tilt angle θ in the fixed magnetic fields (3, 6, and 9 T) and 2 K.

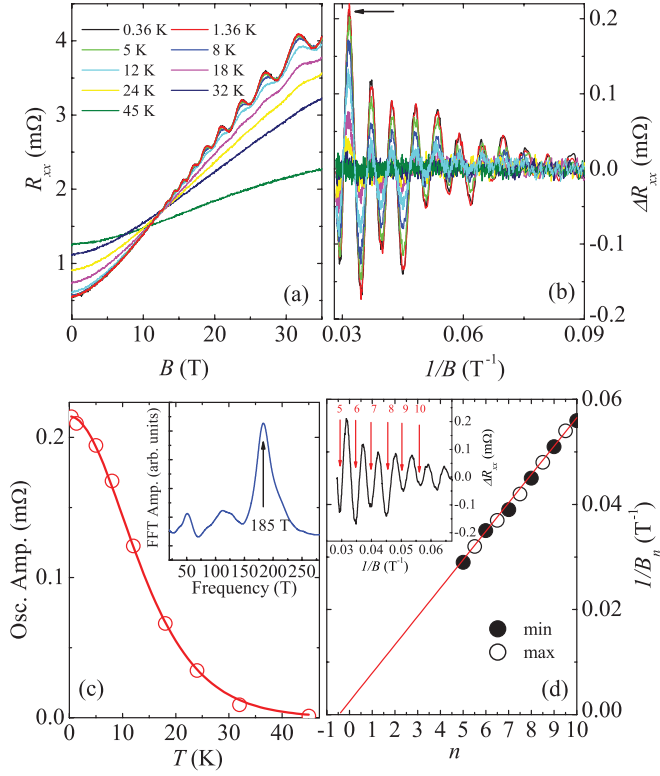


FIG. 3. (Color online) (a) Magnetic field dependence of resistance of CaMnBi_2 crystal and (b) magnetoresistant SdH oscillations $\Delta R_{xx} = R_{xx} - \langle R_{xx} \rangle$ as a function of $1/B$ below 35 T. (c) Temperature dependence of the oscillation amplitude (Osc. Amp.) in magnetoresistant SdH oscillations. The red (light gray) line is the fitting results giving cyclotron mass. The inset shows the Fourier transform spectrum of the SdH oscillation. (d) The integer Landau levels as a function of inverse field. The inset shows the oscillation of ΔR_{xx} at 0.36 K, where the arrows indicate the positions of the estimated LL index n labeled by the numbers.

the MR gradually decreases and becomes nearly negligible for B in the ab plane ($\theta = 90^\circ$). Angular-dependent resistivity in $B = 9$ T and $T = 2$ K shows a wide maximum when the field is parallel to the c axis ($\theta = 0^\circ, 180^\circ$), and a sharper minimum at approximately $\theta = 90^\circ, 270^\circ$ [Fig. 2(a)]. The whole curve follows the function of $|\cos(\theta)|$ very well [red/light gray line in Fig. 2(a)]. The angular-dependent in-plane magnetoresistance suggests a quasi-2D Fermi surface.³

In Figs. 3(a) and 3(b), the in-plane magnetoresistance R_{xx} and the $\Delta R_{xx} = R_{xx} - \langle R_{xx} \rangle$ shows clear Shubnikov-de Hass (SdH) oscillations below 45 K. The Fourier transform spectrum of the oscillation at 0.36 K [inset in Fig. 3(c)] reveals a periodic behavior in $1/B$ with a frequency $F = 185$ T. The temperature dependence of the oscillation amplitude can be used to determine cyclotron effective mass through the Lifshitz-Kosevich formula.²⁶ Using the highest oscillation peak [indicated by the arrow in Fig. 3(b)], the fitting gives a $m \approx 0.35m_e$, where m_e is the bare electron mass [Fig. 3(c)]. In metals, SdH oscillations correspond to successive emptying of LLs as the magnetic field is increased. The LL index n is related to the cross section of FS S_F by $2\pi(n + \gamma) = S_F \frac{\hbar}{eB}$. In the index plot [Fig. 3(d)], the inverse peak and minimum fields $1/B$ fall on a straight line (red/light

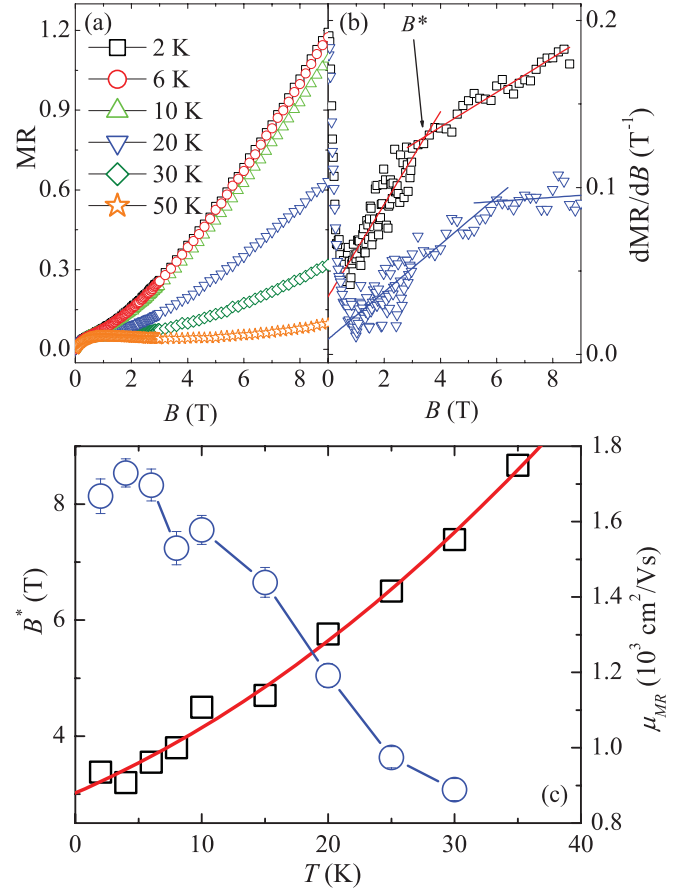


FIG. 4. (Color online) (a) The magnetic field (B) dependence of the in-plane MR at different temperatures. (b) The field derivative of in-plane MR at different temperatures, respectively. The lines in the high-field regions were fitting results using $\text{MR} = A_1 B + O(B^2)$, and the lines in the low-field regions using $\text{MR} = A_2 B^2$. (c) Temperature dependence of the critical field B^* (black squares) and the effective MR mobility μ_{MR} extracted from the weak-field MR (blue circles). The red solid line is the fitting results of B^* using $B^* = \frac{1}{2e\hbar v_F} (E_F + k_B T)^2$.

gray line) versus the integers n and the extrapolation of the high-field SdH peaks and minimum gives $\gamma \simeq 0.45$. γ should be zero for conventional metals but $(\pm)1/2$ for Dirac fermions due to the nonzero Berry's phase associated with their cyclotron motion. The Berry's phase associated with their cyclotron motion. The Berry's phase and the $\sim 1/2$ intercept of the linear fit of LLs have been observed in Dirac fermion systems, such as monolayer graphene¹⁰ and topological insulators.^{12,13} The resulted $\gamma \sim 1/2$, as well as the small cyclotron mass $0.35m_e$, reveals the presence of Dirac fermions in CaMnBi_2 .

Figure 4(a) shows the magnetic field dependence of MR at different temperatures and Fig. 4(b) shows the field derivative of MR, $d\text{MR}/dB$. $d\text{MR}/dB$ initially decreases with an increase in field, indicating the $B^{1/2}$ dependence of MR, and then linearly increases with field in the low-field region, which indicates a B^2 -dependent MR by linear fitting (lines in the low-field region). But above a characteristic field B^* , $d\text{MR}/dB$ saturates to a much reduced slope. This indicates that in the high fields the MR is dominated by a linear field dependence plus a very small quadratic term [$\text{MR} = A_1 B + O(B^2)$], as

shown by the lines in the high-field region. With an increase in temperature, MR decreases and the crossover field B^* increases gradually. Above 50 K, MR becomes negligible. Below 9 T and 50 K, the evolution of B^* with temperature is parabolic [squares in Fig. 4(c)].

The energy splitting between the lowest and first LLs of Dirac fermions can be described by $\Delta_{LL} = \pm v_F \sqrt{2e\hbar B}$, where v_F is the Fermi velocity.¹⁰⁻¹³ In the quantum limit at specific temperature and field, Δ_{LL} becomes larger than both the Fermi energy E_F and the thermal fluctuations $k_B T$ at a finite temperature. Consequently all carriers occupy the lowest Landau level and eventually the quantum transport with linear magnetoresistance shows up. The critical field B^* above which the quantum limit is satisfied at a specific temperature T is $B^* = \frac{1}{2e\hbar v_F} (E_F + k_B T)^2$.¹⁴ The temperature dependence of the critical field B^* in CaMnBi₂ clearly deviates from the linear relationship and can be well fitted by the above equation, as shown in Fig. 4(c). This confirms the existence of Dirac fermion states in CaMnBi₂.

In a multiband system with both Dirac and conventional parabolic-band carriers (including electrons and holes) where the Dirac carriers are dominant in transport, the coefficient of the low-field semiclassical B^2 quadratic term A_2 is related to the effective MR mobility $\sqrt{A_2} = \frac{\sqrt{\sigma_e \sigma_h}}{\sigma_e + \sigma_h} (\mu_e + \mu_h) = \mu_{MR}$ (where $\sigma_e, \sigma_h, \mu_e, \mu_h$ are the effective electron and hole conductivity and mobility in zero field, respectively). The effective MR is smaller than the average mobility of carriers $\mu_{avg} = \frac{\mu_e + \mu_h}{2}$ and gives an estimate of the lower bound.^{14,15} Figure 4(c) shows the dependence of μ_{MR} on the temperature. At 2 K, the value of μ_{MR} is $\sim 1800 \text{ cm}^2/\text{V s}$ in CaMnBi₂, which is larger than the values in conventional metals.

Compared to SrMnBi₂, the effective MR mobility in CaMnBi₂ is smaller ($\sim 3400 \text{ cm}^2/\text{V s}$ in SrMnBi₂), while the crossover field $B^* \sim 3 \text{ T}$ at 2 K and the cyclotron mass $m \sim 0.35m_e$ is larger, implying a smaller Fermi velocity of

Dirac fermions. This may be due to the contribution of the wide parabolic band in CaMnBi₂ [as shown in Fig. 1(d)] which is absent in SrMnBi₂.^{17,18,27} The Berry's phase revealed by the quantum oscillations, combined with the results of our first-principles electronic structure calculations and the quadratic-temperature dependence of the crossover field from semiclassical transport to quantum linear magnetoresistance, provide a convincing evidence for the existence of Dirac fermions in 2D Bi square nets of CaMnBi₂ and SrMnBi₂.²⁷ The direct observation of the linear energy dispersion in Bi square nets and the detailed information on multiband characteristics deserve further study by more powerful spectroscopy methods such as angle-resolved photoemission spectroscopy (ARPES) and will be sought after.

In summary, we report two-dimensional Dirac fermions and quantum magnetoresistance in single crystals of CaMnBi₂. The nonzero Berry's phase, small cyclotron resonant mass, and first-principles band structure suggest the existence of 2D Dirac fermions in Bi square nets. The in-plane transverse magnetoresistance exhibits a crossover at a critical field B^* from a semiclassical weak-field B^2 dependence to the high-field unsaturated linear magnetoresistance ($\sim 120\%$ in 9 T at 2 K) due to the quantum limit of the 2D Dirac fermions. The temperature dependence of B^* satisfies quadratic behavior, which is attributed to the splitting of linear energy dispersion in high field. Our results demonstrate the existence of two-dimensional Dirac fermions in CaMnBi₂ with similar Bi square net structural components.

We thank John Warren for help with SEM measurements. This work was performed at Brookhaven National Laboratory and supported by the US DOE under Contract No. DE-AC02-98CH10886. Work at the National High Magnetic Field Laboratory is supported by the DOE NNSA DE-FG52-10NA29659 (S.W.T. and D.G.), by the NSF Cooperative Agreement No. DMR-0654118, and by the state of Florida.

¹M. B. Salamon and M. Jaime, *Rev. Mod. Phys.* **73**, 583 (2001).

²S. A. Wolf, D. D. Awschalom, R. A. Buhrman, J. M. Daughton, S. von Molnár, M. L. Roukes, A. Y. Chtchelkanova, and D. M. Treger, *Science* **294**, 1488 (2001).

³A. B. Pippard, *Magnetoresistance in Metals* (Cambridge University Press, Cambridge, UK, 1989).

⁴A. A. Abrikosov, *Europhys. Lett.* **49**, 789 (2000).

⁵R. Xu, A. Husmann, T. F. Rosenbaum, M.-L. Saboung, J. E. Enderby, and P. B. Littlewood, *Nature (London)* **390**, 57 (1997).

⁶M. Lee, T. F. Rosenbaum, M.-L. Saboungi, and H. S. Schnyders, *Phys. Rev. Lett.* **88**, 066602 (2002).

⁷F. Y. Yang, K. Liu, D. H. Reich, P. C. Searson, and C. L. Chien, *Science* **284**, 1335 (1999).

⁸A. A. Abrikosov, *Phys. Rev. B* **58**, 2788 (1998).

⁹W. Zhang, R. Yu, W. Feng, Y. Yao, H. Weng, X. Dai, and Z. Fang, *Phys. Rev. Lett.* **106**, 156808 (2011).

¹⁰Y. Zhang, Z. Jiang, Y.-W. Tan, H. L. Stormer, and P. Kim, *Nature (London)* **438**, 201 (2005).

¹¹D. Miller, K. Kubista, G. Rutter, M. Ruan, W. de Heer, P. First, and J. Stroscio, *Science* **324**, 924 (2009).

¹²D.-X. Qu, Y. S. Hor, J. Xiong, R. J. Cava, and N. P. Ong, *Science* **329**, 821 (2010).

¹³J. G. Analytis, R. D. McDonald, S. C. Riggs, J.-H. Chu, G. S. Boebinger, and I. R. Fisher, *Nat. Phys.* **6**, 960 (2010).

¹⁴K. K. Huynh, Y. Tanabe, and K. Tanigaki, *Phys. Rev. Lett.* **106**, 217004 (2011).

¹⁵H.-H. Kuo, J.-H. Chu, S. C. Riggs, L. Yu, P. L. McMahon, K. De Greve, Y. Yamamoto, J. G. Analytis, and I. R. Fisher, *Phys. Rev. B* **84**, 054540 (2011).

¹⁶A. H. Castro Neto, F. Guinea, N. M. R. Reres, K. S. Novoselov, and A. K. Geim, *Rev. Mod. Phys.* **81**, 109 (2009).

¹⁷J. Park, G. Lee, F. Wolff-Fabris, Y. Y. Koh, M. J. Eom, Y. K. Kim, M. A. Farhan, Y. J. Jo, C. Kim, J. H. Shim, and J. S. Kim, *Phys. Rev. Lett.* **107**, 126402 (2011).

¹⁸J. K. Wang, L. L. Zhao, Q. Yin, G. Kotliar, M. S. Kim, M. C. Aronson, and E. Morosan, *Phys. Rev. B* **84**, 064428 (2011).

- ¹⁹P. C. Canfield and Z. Fisk, *Philos. Mag. B* **65**, 1117 (1992).
- ²⁰M. Weinert, E. Wimmer, and A. J. Freeman, *Phys. Rev. B* **26**, 4571 (1982).
- ²¹P. Blaha, K. Schwarz, G. K. H. Madsen, D. Kvasnicka, and J. Luitz, *WIEN2k, An Augmented Plane Wave + Local Orbitals Program for Calculating Crystal Properties* (Karlheinz Schwarz, Techn. Universitat Wien, Austria, 2001).
- ²²J. P. Perdew, K. Burke, and M. Ernzerhof, *Phys. Rev. Lett.* **77**, 3865 (1996).
- ²³E. Brechtel, G. Cordier, and H. Schaffer, *Z. Naturforsch., B* **35**, 1 (1980).
- ²⁴Yogesh Singh, M. A. Green, Q. Huang, A. Kreyssig, R. J. McQueeney, D. C. Johnston, and A. I. Goldman, *Phys. Rev. B* **80**, 100403 (2009).
- ²⁵S. Bobev and J. Merz, *Inorg. Chem.* **45**, 4047 (2006).
- ²⁶D. Shoeneberg, *Magnetic Oscillation in Metals* (Cambridge University Press, Cambridge, UK, 1984).
- ²⁷K. Wang, D. Graf, H. Lei, S. W. Tozer, and C. Petrovic, *Phys. Rev. B* **84**, 220401(R) (2011).